South China Sea Wind-Wave Characteristics. Part I: Validation of Wavewatch-III Using TOPEX/Poseidon Data

PETER C. CHU

Naval Ocean Analysis and Prediction Laboratory, Department of Oceanography, Naval Postgraduate School, Monterey, California

YIQUAN QI

South China Sea Institute of Oceanology, Chinese Academy of Sciences, Guangzhou, China

YUCHUN CHEN

Cold and Arid Regions Environmental and Engineering Research Institute, Chinese Academy of Sciences, Lanzhou, China

PING SHI AND QINGWEN MAO

South China Sea Institute of Oceanology, Chinese Academy of Sciences, Guangzhou, China

ABSTRACT

A full-spectral third-generation ocean wind-wave model, Wavewatch-III, has been implemented in the South China Sea (SCS) for investigating wind-wave characteristics. This model was developed at the Ocean Modeling Branch of the National Centers for Environmental Prediction (NCEP). The NASA QuickSCAT data (0.25° resolution) 2 times daily were used to simulate the wind waves for the entire year of 2000. The significant wave heights from Wavewatch-III are compared to the TOPEX/Poseidon (T/P) significant wave height data over the satellite crossover points in SCS. The model errors of significant wave height have Gaussian-type distribution with a small mean value of 0.02 m (almost no bias). The model errors are comparable to the T/P altimeter accuracy (0.5 m) in the central SCS and are smaller than the T/P altimeter accuracy in the northern and southern SCS, which indicates the capability of Wavewatch-III for SCS wave simulation.

1. Introduction

The South China Sea (SCS) is a semienclosed tropical sea located between the Asian landmass to the north and west, the Philippine Islands to the east, Borneo to the southeast, and Indonesia to the south (Fig. 1), a total area of 3.5×10^6 km². It connects to the East China Sea (through Taiwan Strait), the Pacific Ocean (through Luzon Strait), the Sulu Sea, the Java Sea (through Gasper and Karimata Straits), and to the Indian Ocean (through the Strait of Malacca). All of these straits are shallow except Luzon Strait, the maximum depth of which is 1800 m. The elliptically shaped central deep basin is 1900 km along its major axis (northeast–southwest) and approximately 1100 km along its minor axis, and extends to over 4000 m deep.

The SCS is under the influence of monsoon winds and synoptic systems such as fronts and tropical cyclones (Chu et al. 1999a,b, 2000). From November to March, the northeasterly winter monsoon winds correspond to monthly mean January 2000 wind speeds of near 10 m s^{-1} for the whole SCS (Fig. 2a). From April to August, the southwesterly summer monsoon winds result in monthly mean July 2000 wind speeds of approximate 8 m s^{-1} in the southern SCS and 4 m s^{-1} in the northern SCS (Fig. 2b). The monthly mean winds (Fig. 2) are typical for monsoon winds. Highly variable winds and surface currents are observed during the transitional periods. Moreover, synoptic systems often pass by the SCS and cause temporally and spatially varying wind fields.

A fully spectral third-generation ocean wind-wave model, Wavewatch-III (henceforth denoted as WWATCH), has been recently developed at the Ocean Modeling Branch of the Environmental Modeling Center of the National Centers for Environmental Prediction (NCEP) for the regional sea wave prediction. It was built on the base of Wavewatch-I and Wavewatch-II as developed at the Delft University of Technology and the National Aeronautics and Space Administration (NASA)

Corresponding author address: Peter C. Chu, Dept. of Oceanography, Naval Postgraduate School, Monterey, CA 93943.
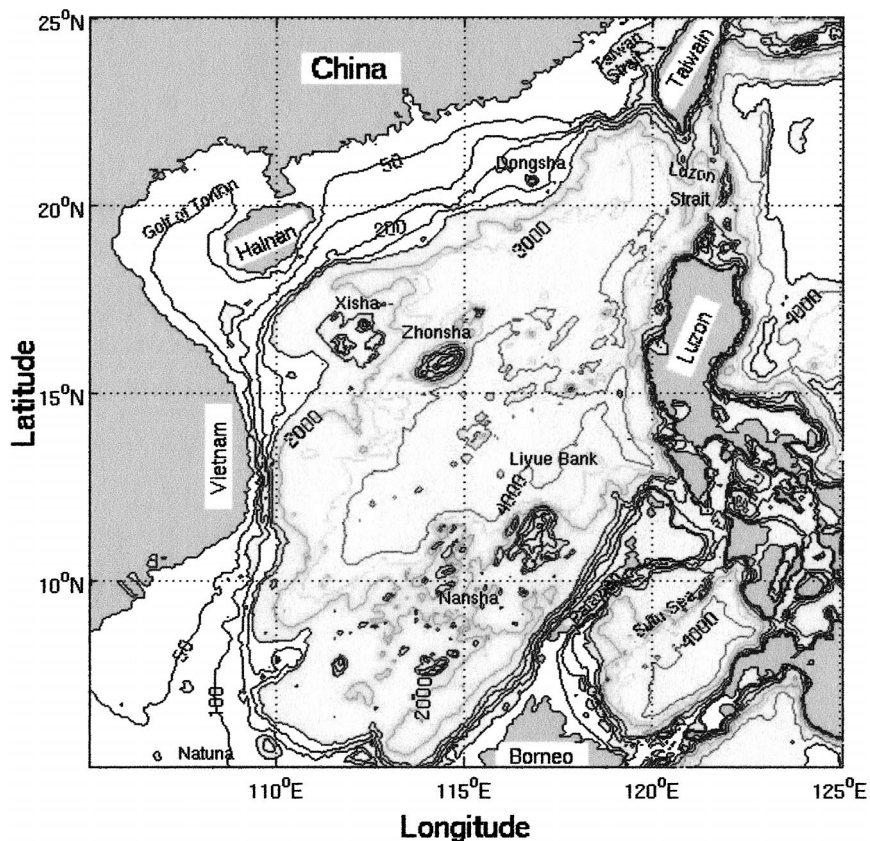E-mail: chu@nps.navy.mil

FIG. 1. Geography and isobaths showing the bottom topography of the South China Sea.

Goddard Space Flight Center, respectively (Tolman 1999).

WWATCH should be evaluated before the practical use. The highly variable wind systems and complicated topography make SCS a perfect location for WWATCH evaluation. Usually the in situ wind-wave data are mainly collected from voluntary ships and wave buoys. However, in the SCS sparse voluntary ship data and no wave buoy data are available. Remote sensing is an important source for the wind-wave data. Several satellites have been launched with altimetry, such as the TOPEX/Poseidon (T/P) satellite and the European Remote Sensing Satellites *ERS-1/2*. The subsequent sections describe the WWATCH evaluation using the T/P significant wave height (SWH) data.

The outline of this paper is as follows. A description of data and WWATCH is given in sections 2 and 3. Methodology and model evaluation are given in sections 4 and 5. In section 6, we present our conclusions.

2. Data

a. T/P SWH and wind speed

The T/P satellite, jointly launched by NASA and the French Space Agency, the Center National d'Etudes Spatiales (CNES), in August 1992, carried a state-of-the-art radar altimetry system (Fu et al. 1994). In addition to precise measurements of the distance between the satellite and the surface, SWH and wind speed are derived from the shape of the leading edge of the returning radar pulse. The accuracy of SWH measurement by T/P was within the accuracy of the *Geosat* measurements (Callahan et al. 1994), that is, 10% or 0.5 m, whichever is greater (Dobson et al. 1987). The T/P satellite was maneuvered into a 9.9156-day repeat period during which two T/P SWH and wind speed data are available at each crossover point. Time series of SWH at 20 crossover points (Fig. 3a) and at four tracks (051, 229, 152, 190 in Fig. 3b) for 2000 are used to evaluate WWATCH.

b. QuikSCAT sea surface winds

NASA launched the microwave scatterometer SeaWinds on the *QuikBird* satellite in June 1999. This instrument is referred to as QuikSCAT (or QSCAT). QSCAT is essentially a radar device that transmits radar pulses down to the earth's surface and then measures the power that is scattered back to the instrument. This "backscattered" power is a measure of surface roughness. For water surfaces, the surface roughness is highly correlated with the near-surface wind speed and direction. Hence, wind speed and direction at a height of
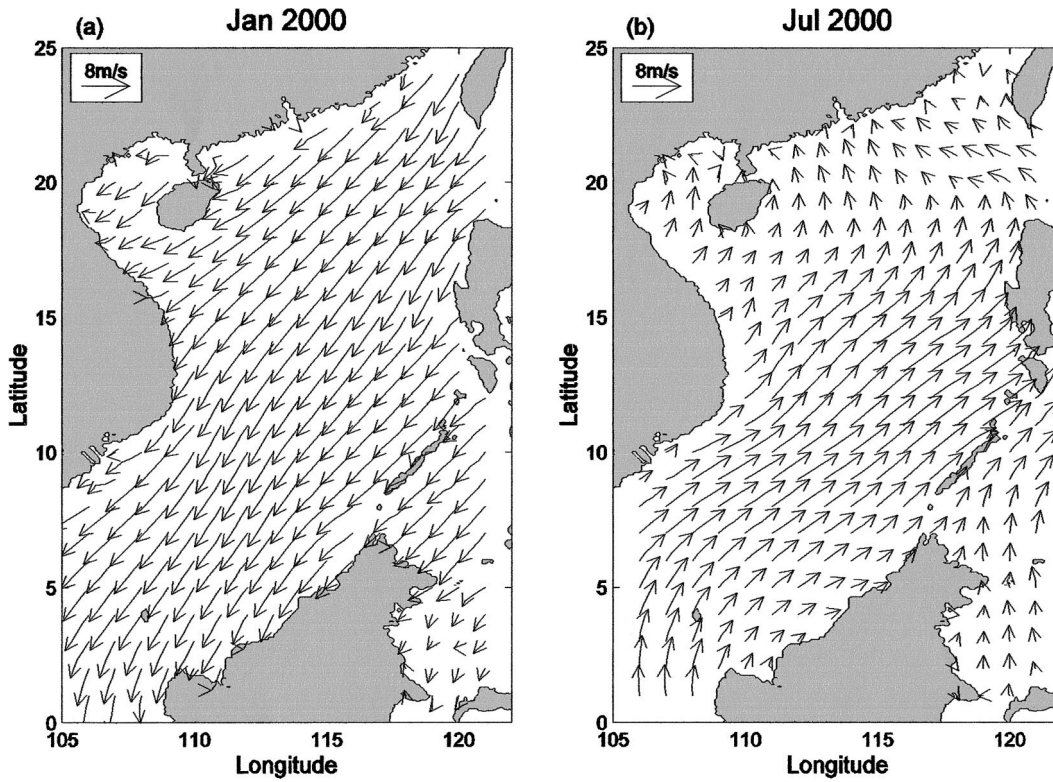
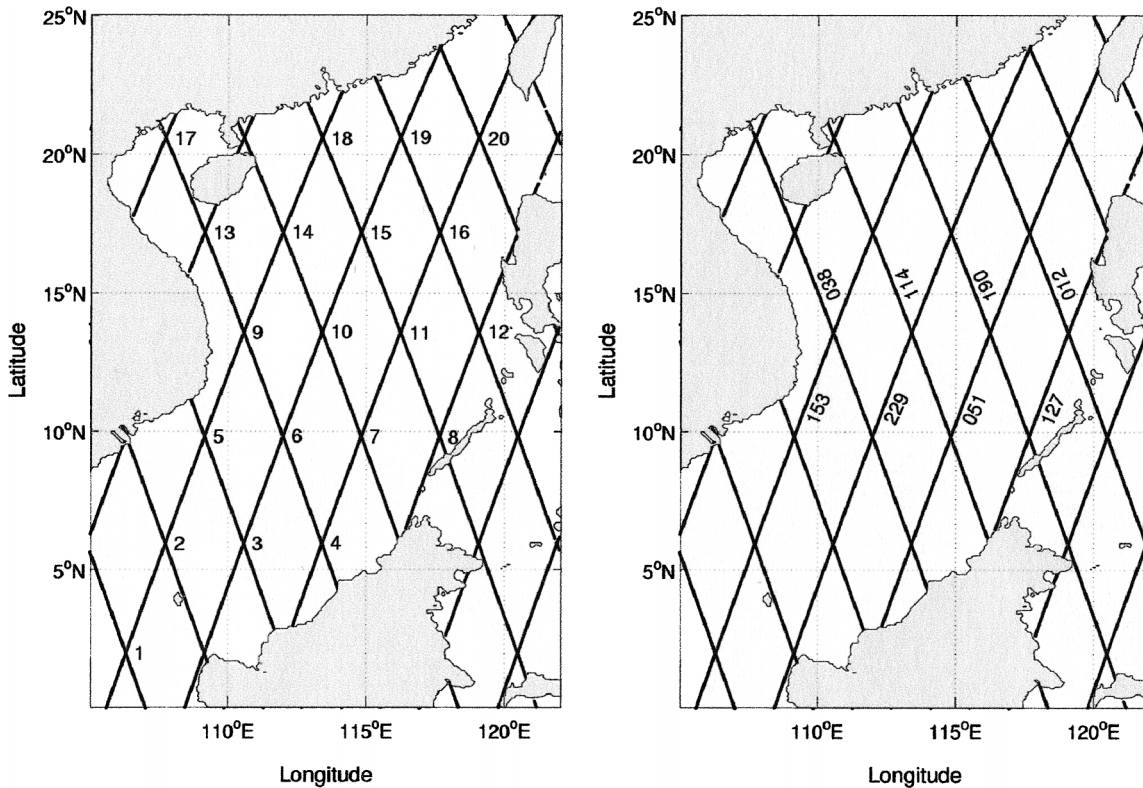FIG. 2. Monthly mean wind speed at 10-m height computed from the QSCAT data: (a) Jan and (b) Jul 2000.

FIG. 3. The T/P satellite (a) crossover points and (b) tracks in the SCS.

TABLE 1. Model setting for this study.

Switch parameter	Characteristics
DUM	Dummy to be used if WWATCH is to be installed on previously untried hardware
LRB8	8-byte words
SHRD	Shared memory model, no message passing
SEED	Seeding of high-frequency energy
GRD1	Settings directly hardwired to user-defined spatial grids (spherical coordinate with 0.25° grids)
SP1	User-defined spectral grids
PR2	Ultimate quickest propagation scheme with Booij and Holthuijsen (1987) dispersion correction
ST2	Tolman and Chalikov (1996) source term package
STAB2	Enable stability correction for Tolman and Chalikov (1996) source term package
NL1	Nonlinear interaction (DIA)
BT1	JONSWAP bottom friction formulation
WIND2	Approximately quadratic interpolation
CUR2	Approximately quadratic interpolation
o1	Output of boundary points in grid preprocessor
o2	Output of the gridpoint status map in grid preprocessor
o2a	Generation of landsea mask file mask.ww3 in grid preprocessor
o3	Additional output in loop over fields in field preprocessor
o4	Print plot of normalized 1D energy spectrum in initial conditions program
o5	2D energy spectrum
o6	Spatial distribution of wave heights (not adapted for distribution memory)
o7	Echo input data for homogeneous fields in generic shell

10 m over the ocean surface are retrieved from measurements of the QSCAT backscattered power. The backscattered power is also affected by rain.

The QSCAT Level-3 global surface wind dataset consists of twice-daily gridded values ($0.25° \times 0.25°$) of scalar wind speed, meridional and zonal components of wind velocity, wind speed squared, and time given in fraction of a day. The presence of rain may degrade the accuracy of the QSCAT winds. Such degradation is indicated by rain probability determined using the multidimensional histogram (MUDH) rain flagging technique. Data are currently available in hierarchical data format (HDF) and exist from 19 July 1999 to the present.

3. WWATCH model

a. Description

The wave spectrum F is generally a function of all phase parameters (i.e., wavenumber k, direction θ, intrinsic frequency σ, and absolute frequency ω), space ($\mathbf{x}$), and time (t):

$$F = F(k, \theta, \sigma, \omega; \mathbf{x}, t).$$

However, the individual spectral components are usually assumed to satisfy the linear wave theory (locally) and to follow the dispersion relation,

$$\sigma^2 = gk \tanh kd \tag{1}$$

$$\omega = \sigma + \mathbf{k} \cdot \mathbf{U}, \tag{2}$$

where d is the mean water depth and $\mathbf{U}$ is the (depth and time averaged) current velocity. When the current velocity vanishes, only two-phase parameters among (σ, k, θ) are independent. Current wave models use the frequency direction (σ, θ) as the independent phase variables.

WWATCH uses the wavenumber direction (k, θ) as the independent phase variables. Without currents, the energy of a wave package is conserved. With currents the energy of a spectral component is no longer conserved (Longuet-Higgins and Stewart 1961), but the wave action spectrum, $N(k, \theta; \mathbf{x}, t) \equiv F(k, \theta; \mathbf{x}, t)/\sigma$, is conserved (Whitham 1965; Bretherthon and Garrett 1968). In WWATCH, the balance equation is for the wave action spectrum.

b. Model setting

WWATCH has two types (mandatory and optional) of model switches for users to choose. Table 1 lists the model setting and optional switches for this study. For example, spatial and spectral grids are user defined; the ultimate quickest propagation scheme is selected with the dispersion correction from Booij and Holthuijsen (1987); nonlinear interactions are included; and the source term parameterization, following Tolman and Chalikov (1996), consists of four parts: wind input, nonlinear wave–wave interaction, dissipation, and wave–bottom interaction. The output of WWATCH consists of the traditional frequency-direction spectrum $F(\sigma, \theta)$, which is calculated from $F(k, \theta)$ using Jacobean transformations.

c. Discretization

The model is implemented for SCS (0°–25°N, 105°–122°E) using realistic bathymetry data from the Naval Oceanographic Office DBDB5 database and a regularly spaced latitude–longitude grid with the grid spacing 0.25° (i.e., $\Delta \lambda = \Delta \phi = 0.25°$).

The wavenumber grid spacing is determined by the frequency intervals (total 25)

$$\sigma_{m+1} = X_\sigma \sigma_m, \quad m = 0, 1, \ldots, 24, \tag{3}$$

with

$$X_\sigma = 1.1, \qquad \sigma_0 = 0.0418. \tag{4}$$

The wave direction (θ) grid spacing is 15° (i.e., $\Delta\theta = 15°$).

Four time steps are used in WWATCH to reach computational efficiency: (a) a global time step (300 s) for the propagation of the entire solution, (b) a spatial time step (300 s) representing the spatial propagation, (c) a spectral time step (300 s) for intraspectral propagation, and (d) a source time step (100 s) for the source term integration.

d. Wind input and friction velocities

The surface winds (W) at each source time step (100 s) for the year 2000 is interpolated from NASA SeaWinds on twice-daily QuikSCAT (QSCAT) Level-3 gridded ocean wind vectors with 0.25° horizontal resolutions. The friction velocities are needed for the input source function S_{in}. In WWATCH, the friction velocity (u_*) is computed from the wind speed (W) at a given reference height z_r, in terms of a drag coefficient C_r (Tolman and Chalikov 1996):

$$u_*^2 = C_* W^2(z_r). \tag{5}$$

An iteration process is adopted to obtain u_*. Wu's (1982) empirical relation

$$
\begin{aligned}
C_D(W) &= 1.2875 \times 10^{-3} & W < 7.5 \text{ m s}^{-1}, \\
C_D(W) &= (0.8 + 0.065W) \times 10^{-3} & W \geq 7.5 \text{ m s}^{-1},
\end{aligned}
\tag{6}
$$

is used to obtain

$$u_*^{(0)} = \sqrt{C_D} W(z_{10}), \tag{7}$$

as the first-guess friction velocity. Here, $z_{10} = 10$ m. The iteration stops when the change of the friction velocity is smaller than a prescribed criterion. Such iterations are performed during the model initialization but are not necessary during the actual model run, as u_* changes slowly (Tolman 1999). The effect of the atmospheric instability on the friction velocity is parameterized using an effective wind speed W_e (Tolman and Booij 1998), which depends on the surface air and sea temperature difference.

e. Model integration

WWATCH is integrated with twice-daily gridded QSCAT ocean wind vectors (0.25°) from the Joint North Sea Wave Project (JONSWAP) 1973 wave spectra (Hasselmann et al. 1980) on 3 January (no sufficient wind data on 1–2 January for SCS) until 31 December 2000. The model SWH data are interpolated into the T/P crossover points. At each crossover point, there are M pairs (approximately 72) of modeled (H_m) and observed (H_o) SWH data in 2000 (around two pairs per 10 days).

4. Methodology of verification

a. Verification at crossover points

The difference of the modeled and observed SWH,

$$\Delta H = H_m(x, y, t) - H_o(x, y, t), \tag{8}$$

represents the model error. Bias, root-mean-square error (rmse), and correlation coefficient (cc) for each crossover point

$$\text{bias}(x, y) = \frac{1}{M} \sum_{i=1}^{M} \Delta H(x, y, t_i), \tag{9}$$

$$\text{rmse}(x, y) = \sqrt{\frac{1}{M} \sum_{i=1}^{M} [\Delta H(x, y, t_i)]^2}, \tag{10}$$

$$\text{cc}(x, y) = \frac{\sum_{i=1}^{M} [H_m(x, y, t_i) - \overline{H}_m(x, y)][H_o(x, y, t_i) - \overline{H}_o(x, y)]}{\sqrt{\sum_{i=1}^{M} [H_m(x, y, t_i) - \overline{H}_m(x, y)]^2} \sqrt{\sum_{i=1}^{M} [H_o(x, y, t_i) - \overline{H}_o(x, y)]^2}}, \tag{11}$$

are used to verify WWATCH. Here $\overline{H}_m(x, y)$ and $\overline{H}_o(x, y)$ are temporal mean modeled and observed SWH,

$$\overline{H}_m(x, y) = \frac{1}{M} \sum_{i=1}^{M} H_m(x, y, t_i),$$

$$\overline{H}_o(x, y) = \frac{1}{M} \sum_{i=1}^{M} H_o(x, y, t_i), \tag{12}$$

at the crossover points. The T value,

$$T = \frac{\text{cc}\sqrt{M - 2}}{\sqrt{1 - \text{cc}^2}}, \tag{13}$$

with the degrees of freedom of ($M - 2$) is used for the significant test of the correlation coefficient.
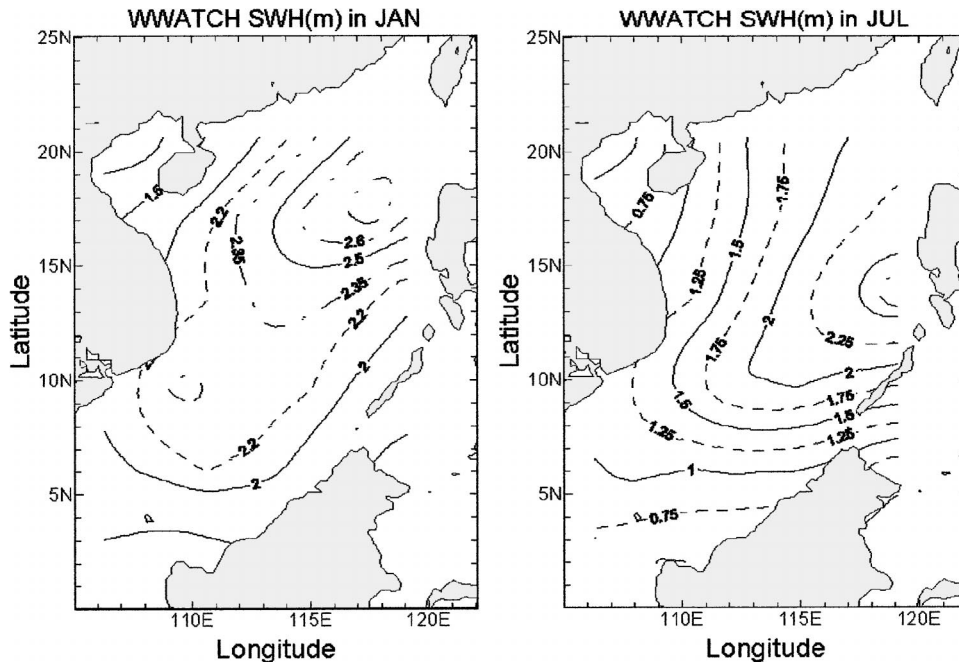
FIG. 4. Simulated monthly mean SWH using WWATCH: (a) Jan and (b) Jul 2000.

b. Verification at time instance

Bias and rmse for time instance t

$$\text{bias}(t) = \frac{1}{N} \sum_{j,k} \Delta H(x_j, y_k, t), \qquad (14)$$

$$\text{rmse}(t) = \sqrt{\frac{1}{N} \sum_{j,k} [\Delta H(x_j, y_k, t)]^2}, \qquad (15)$$

are also used to verify WWATCH.

5. Model results

Two types of model–observation comparison are conducted: 1) horizontal SWH pattern using monthly mean data and 2) model error statistics using synoptic crossover point SWH data (model and observation). To show the value added by using WWATCH, the Pierson–Moskowitz (P–M) spectrum (Pierson and Moskowitz 1964) is also used for comparison in monthly mean horizontal SWH pattern.

a. Monthly mean SWH

Three sets of monthly mean data are calculated from (a) modeled SWH using WWATCH, (b) calculated SWH using the P–M spectrum with the same QSCAT winds, and (c) observed SWH from T/P. A common feature in the simulated (Fig. 4), calculated (Fig. 5), and observed (Fig. 6) data shows a higher SWH in January 2000 than in July 2000.

In January 2000, a southwest-to-northeast-oriented high-SWH region (>2.0 m) is comparable (north of 5°N)

in the WWATCH simulation (Fig. 4a) and in the T/P data (Fig. 6a). However, this high-SWH region is split into two smaller ones in the calculated (from P–M spectrum) field, with a major one occurring north of 15°N and a minor one near the southern Vietnamese coast (Fig. 5a). The area with SWH larger than 2.5 m in the WWATCH simulation (15°–20°N, 113°–117°E) is comparable to that in the T/P data (13°–20°N, 112°–117°E). Due to its independence on fetch, the P–M results show the SWH maximum of 3 m near the northeast boundaries (upwind), which is not found in the simulated (WWATCH) and observed fields.

In July 2000, the mean SWHs are higher in the northern and central SCS (north of 10°N) than in the southern SCS (south of 10°N), with values larger than 2.25 m in the WWATCH simulated field (Fig. 4b) and larger than 2.5 m in the calculated (from the P–M spectrum) (Fig. 5b) and observed fields (Fig. 6b). However, the maximum SWH values are located at 11°–15°N, 115°–120°E in simulated and calculated fields and at 15°–20°N, 113°–116°E in the observed field.

Due to its independence on fetch, the P–M results show the SWH maximum of 3 m near the northeast boundaries (upwind) in January and of 2 m near the southern boundaries (upwind) in July, which is not found in the simulated (WWATCH) and observed fields. WWATCH simulates the seasonal variability of SWH reasonably well. SWH is larger in the winter than in the summer monsoon season. The orientation of the high-SWH region coincides with the orientation of the monsoon winds (Fig. 2). The observed data show some more intensification in the maximum values. The SWHs show more irregular pat-
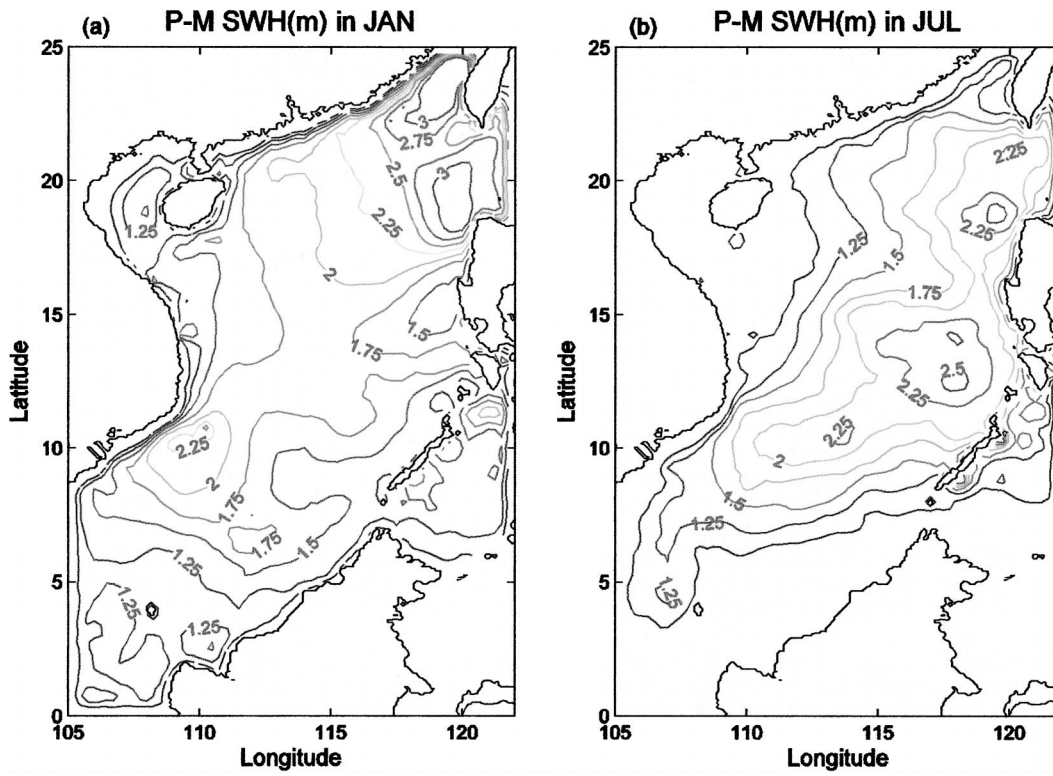
FIG. 5. Calculated monthly mean SWH using the Pierson–Moskowitz spectrum: (a) Jan and (b) Jul 2000.
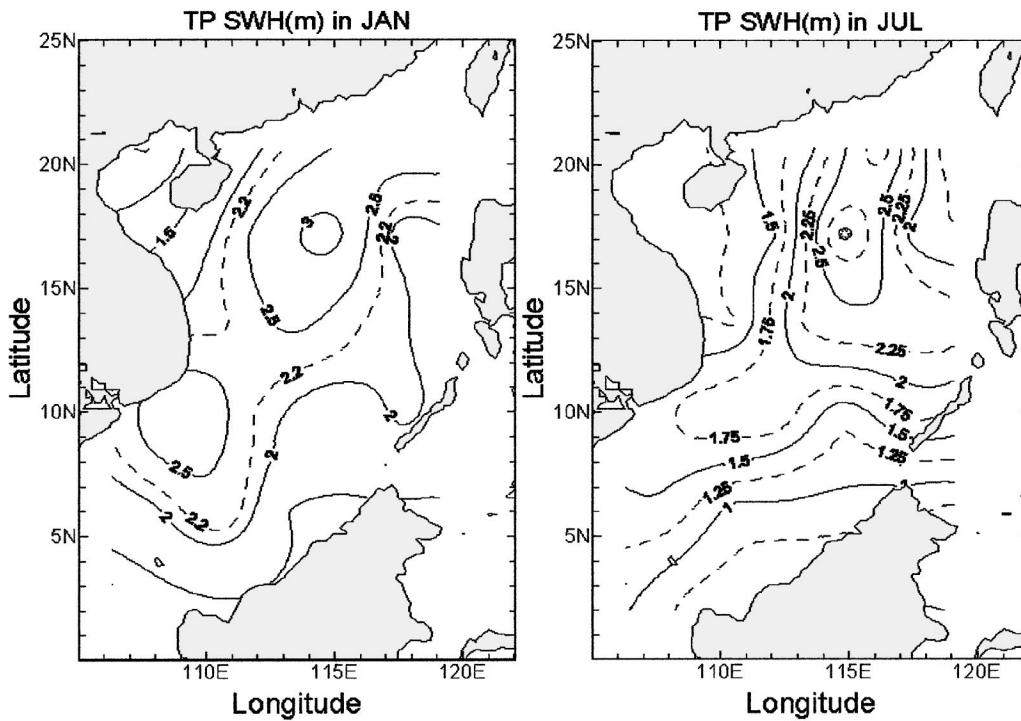

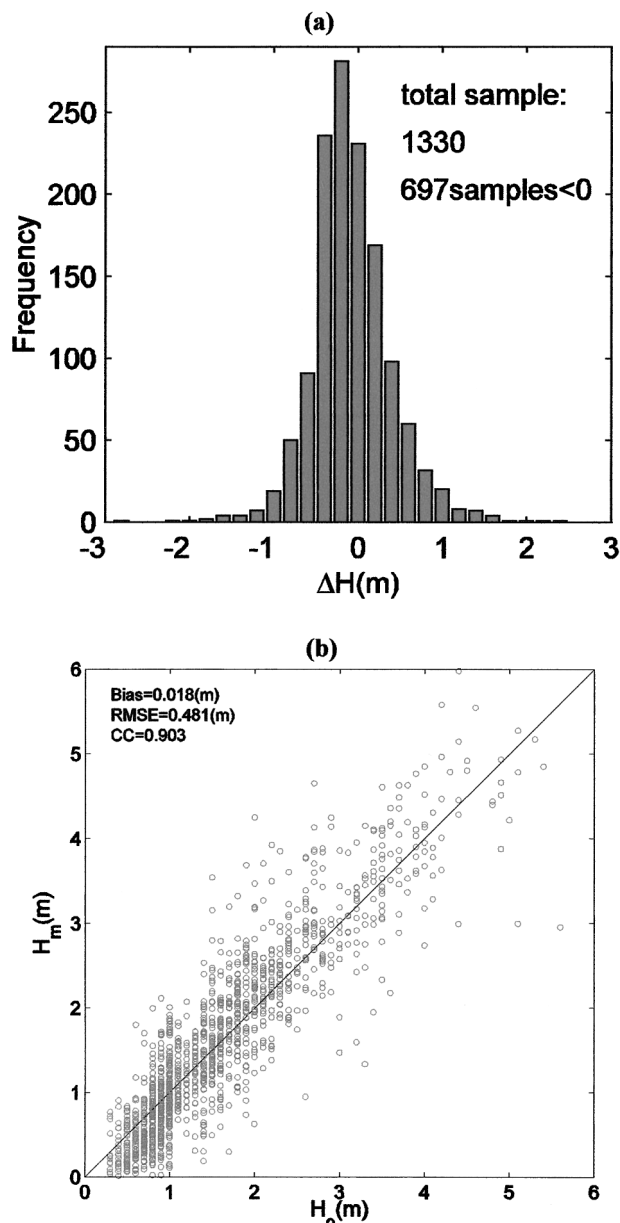FIG. 6. Monthly mean SWH from T/P data: (a) Jan and (b) Jul 2000.

(a)

(b)

FIG. 7. Model accuracy statistics: (a) histogram of model error and (b) scatter diagram of modeled (H_m) and observed (H_o) SWH for all the crossover points.

terns using the P–M spectrum than using WWATCH. This is due to the coarse resolution in time of the wind input (twice daily) that smoothes out extremes such as storm event (Chu et al. 2000; Chen et al. 2002).

b. Statistical evaluation

The model–observation comparison is conducted at all 20 crossover points in the SCS. Each one contains approximate 72 pairs of modeled (H_m) and observed (H_o) SWH data in 2000. The total number of pairs is 1330. The difference between the two, $\Delta H = H_m - H_o$, is

considered as the model error. The histogram of $\Delta H = [= H_m - H_o]$ (Fig. 7a) for all 20 crossover points shows a Gaussian-type distribution with mean value (-0.02 m) and with comparable sample numbers of positive ΔH (633) with negative ΔH (697). The scatter diagrams for H_m and H_o show clustering of points approximately around the line of $H_m = H_o$ (Fig. 7b). The rmse and cc between H_m and H_o are 0.48 m and 0.90, respectively.

The scatter diagrams for H_m and H_o at each crossover point (Fig. 8) show spatial variability of the error statistics. The rmse increases from 0.34 m at the southwest corner of the SCS near Natuna Island [point 1 (2.01°N, 106.31°E)] to 0.95 m in the central SCS near Zhongsha Island [point 15 (17.18°N, 114.81°E)] and west of Luzon [point 16 (17.20°N, 117.65°E)]. The bias varies from -0.45 m in the Gulf of Tonkin [point 17 (20.59°N, 107.73°E)] to 0.33 m at the southern SCS near Nansha Island [point 7 (9.8°N, 114.81°E)]. The correlation coefficient increases from 0.55 in the Gulf of Tonkin (point 17) to 0.95 in the central SCS near Zhongsha Island (point 15).

Contours of bias, rmse, and cc for the entire year of 2000 are plotted (Fig. 9) to understand the spatial error variability. A positive bias occupies a large portion of the SCS. The zero-bias contour follows 200-m bathymetry (Fig. 1) with negative bias on the continental shelf (west of the zero-bias contour) and positive bias in the deep basin (east of the zero-bias contour). A negative bias larger than -0.4 m is found in the Gulf of Tonkin and a positive bias larger than 0.3 m is located near Nansha Island (10°N, 115°E) (Fig. 9a). This indicates that WWATCH overpredicts the SWH slightly except on the shallow continental shelf. The rmse of SWH is above 0.5 m in the central SCS, with a maximum larger than 0.6 m west of Palawan (Fig. 9b). The value of rmse decreases from the central SCS to the other two regions and is smaller than 0.5 m in most of the northern (west of Luzon) and southern (south of 5°N) SCS.

Strong negative bias in the Gulf of Tonkin is obtained on the basis of observations at a single crossover point (i.e., point 17), which is quite close to the coast. The T/P altimeter data are not as valuable as in the deep sea. Recently, two high-kinetic-energy zones were identified as tidal fronts in the Qiongzhou Strait and near the southwestern coast of the Hainan Island (Hu et al. 2003). Tidal effect is not available in the model simulation.

The cc of SWH (Fig. 9c) between modeled and T/P data in 2000 is larger than 0.85 almost everywhere in the SCS, except in the Gulf of Tonkin. The T value computed using (13) for cc = 0.85, $M = 72$ is $T = 13.50$. For confidence coefficient $(1 - \alpha) = 0.095$, the t distribution for the degree of freedom of statistics for $(M - 2 = 70)$ is $2.756 > t_{0.005} > 2.576$. Since $T(= 13.50)$ is larger than $t_{0.005}$, the correlation coefficient between modeled and T/P SWH data is significant.
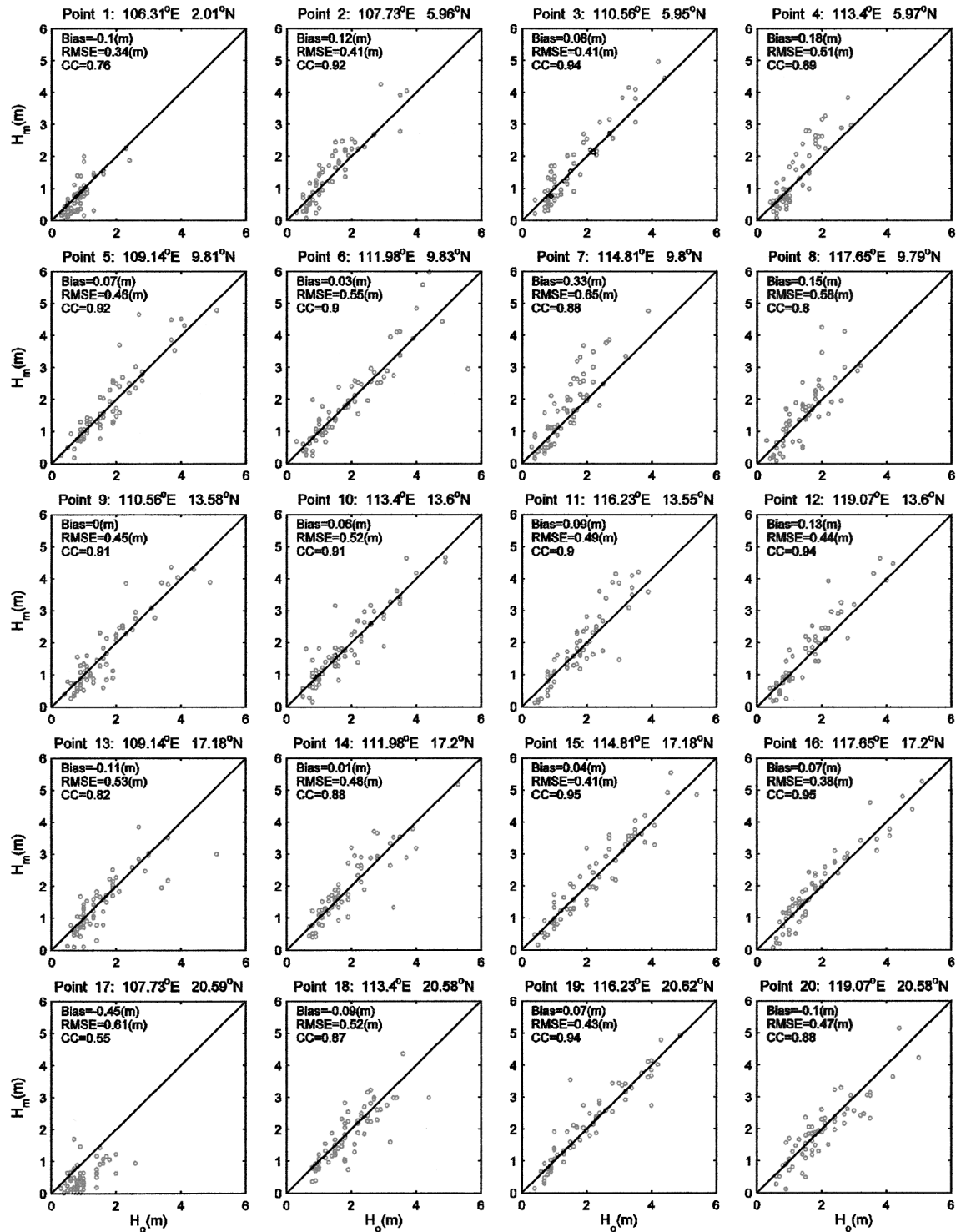
FIG. 8. Scatter diagrams of SWHs at crossover points in the SCS.

c. Spatial error variability along three ascending tracks

Understanding the spatial error variability during different periods, four tracks (051, 229, 153, 190; see Fig. 3b) covering the SCS and three cycles (270, 288, 302) are selected for the model evaluation. For each cycle, the T/P SWHs and wind speeds along the tracks are compared to the model-simulated SWHs and QSCAT wind speeds (interpolated with the same temporal resolution with the T/P SWH and wind speed data).
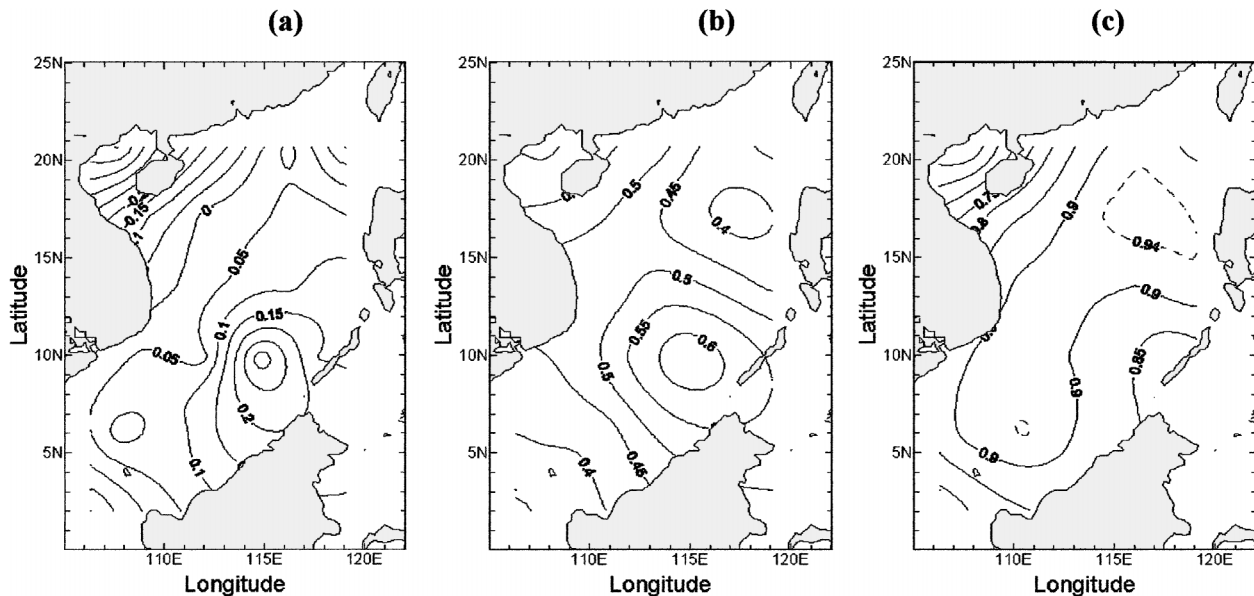
FIG. 9. Distributions of SWH (a) bias, (b) rms error, and (c) correlation coefficient between WWATCH and T/P altimeter data for the entire year of 2000.

1) WINTER MONSOON SEASON (CYCLE 270)

During cycle 270, the T/P satellite passed over tracks 051, 153, 190, and 229 on 14, 18, 19, and 21 January, respectively. The simulated and observed SWHs on the four tracks are presented in the left-hand panels of Fig. 10. The QSCAT and T/P wind speeds on the four tracks are presented in the right-hand panels.

Along tracks 051, 229, and 190 (eastern and middle SCS) the simulated SWH coincides with T/P SWH quite well south of 12°N, with errors usually less than 0.3 m, and deviates from T/P SWH north of 12°N, with errors larger than 1.0 m. Along track 153 (western SCS) the simulated SWH is quite different from T/P SWH, with errors larger than 1.0 m except for the 10°–18°N segment.

After the gridded QSCAT winds are interpolated temporally at each source time step (100 s), the QSCAT and T/P wind speed pairs can be easily obtained along the T/P tracks with no spatial and temporal lags. QSCAT wind speeds agree with T/P wind speeds quite well along the tracks where the wind speed does not have strong spatial variability, such as along track 190. QSCAT wind speeds have a large discrepancy along track 153 south of 10°N and track 229 north of 20°N, where the wind speed has strong spatial variability, with a difference up to around 3–4 m s^{-1}. Comparison between left- and right-hand panels shows that discrepancy in SWH is correlated with wind speed error, except along track 229, where the model errors do not well correlate to the wind errors. This may imply the importance of other source functions such as dissipation and nonlinear effect.

2) SUMMER MONSOON SEASON (CYCLE 288)

During cycle 288, the T/P satellite passed over tracks 051, 153, 190, and 229 on 10, 14, 16, and 17 July, respectively. The simulated and observed SWHs on the four tracks are presented in the left-hand panels of Fig. 11. The QSCAT and T/P wind speeds on the four tracks are presented in the right-hand panels. Along tracks 153 and 229 the simulated SWH coincides with T/P SWH quite well, with errors less than 0.5 m in most of latitudes. Along tracks 051 and 190 the simulated SWH is quite different from T/P SWH, with errors larger than 1.0 m in most latitudes.

QSCAT wind speeds agree with T/P wind speeds quite well along track 153, which leads to a better SWH simulation along that track. QSCAT wind speeds have a large discrepancy from the T/P wind speeds along track 153, which leads to larger SWH errors along that track. Thus, the summer monsoon winds seem more difficult to resolve in the model. Quality of the wind input is important for SWH prediction.

3) TROPICAL STORM RUMBIA 2000 (CYCLES 302 AND 303)

Cycles 302 and 303, during which Tropical Storm Rumbia 2000 was passing SCS with maximum guess strength of 25–30 m s^{-1}, are selected for evaluation of model capability under strong and highly varying wind forcing. Tropical Storm Rumbia initially formed about 800 km east of the Philippine island of Mindanao on 28 November 2000 (Fig. 12). After formation, Rumbia slowly intensified as it tracked westward through the Philippine Sea toward the central Philippine Islands. On
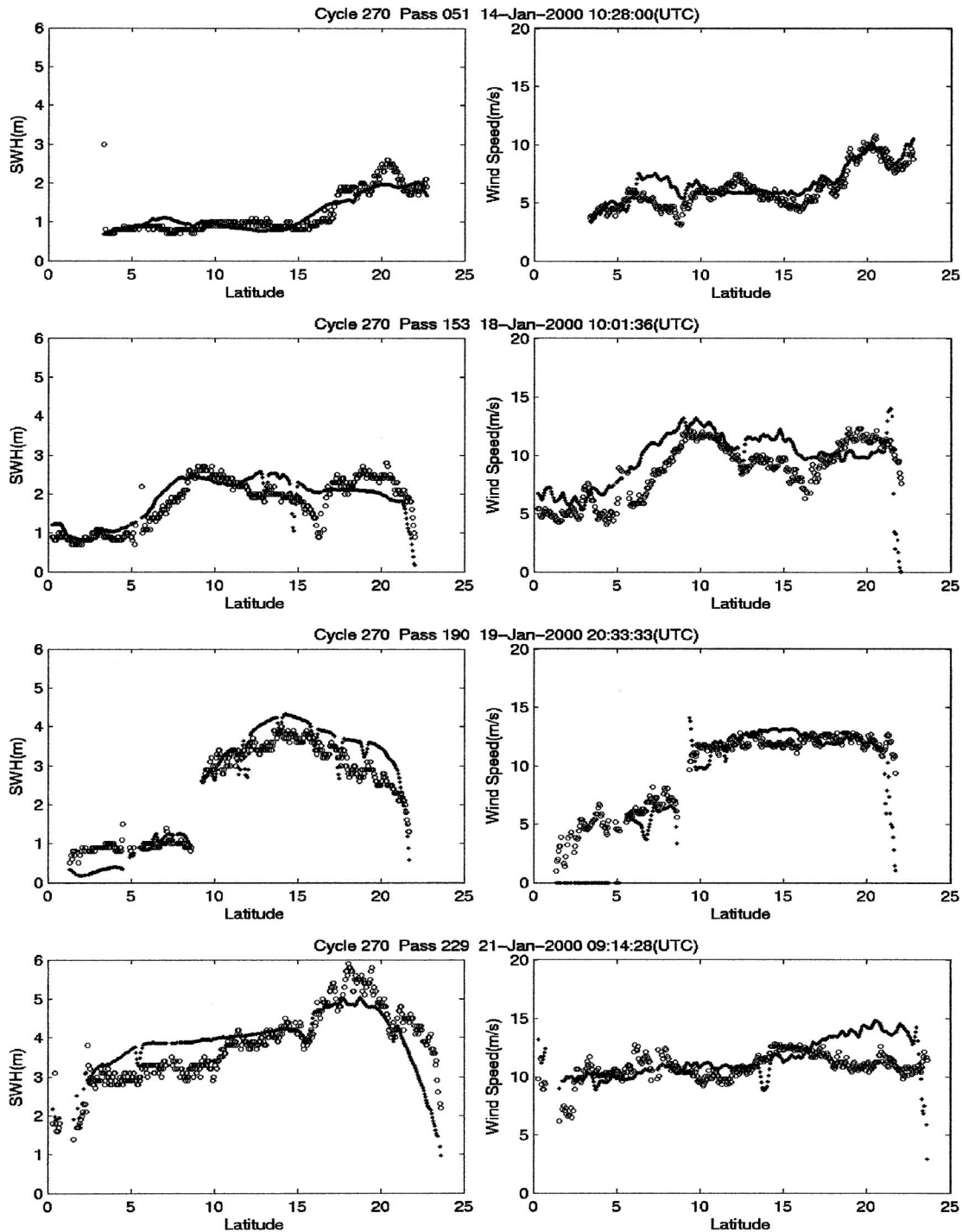
FIG. 10. Comparison between (left) modeled (dotted) and T/P observed (circle) SWHs and (right) QSCAT (dotted) and T/P observed wind speeds (circle) along the four tracks during cycle 270 (14–21 Jan 2000).

1 December, it made landfall over the eastern Philippines and intensified to tropical storm strength, 18 m s^{-1} (measured by QSCAT). It continued moving westerly through the Philippine Islands, intensifying at a slow rate. After it entered the SCS, it continued to move westward, and weakened and disappeared on 9 December 2000 near the southern tip of Vietnam.

The T/P satellite passed over track 190 (2 December) and track 229 (3 December) during cycle 302, and over track 051 (6 December) and track 153 (10 December) during cycle 303. The simulated and observed SWHs (from T/P altimeter) on the four tracks are presented in the left-hand panels of Fig. 13. The QSCAT and T/P wind speeds on the four tracks are presented in the right-
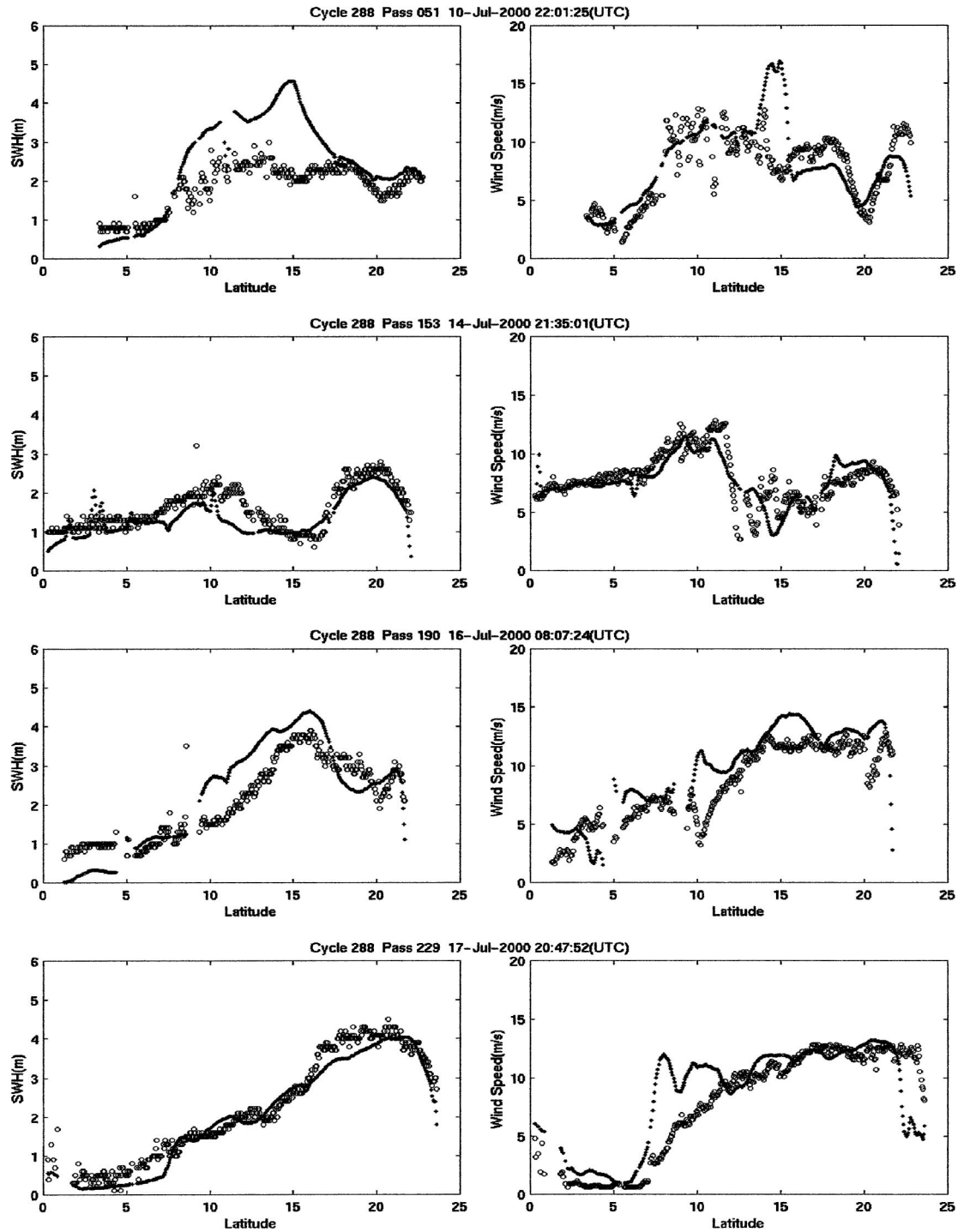
FIG. 11. Comparison between (left) modeled (dotted) and T/P observed (circle) SWHs and (right) QSCAT (dotted) and T/P observed wind speeds (circle) along the four tracks during cycle 288 (10–17 Jul 2000).

hand panels. Along track 190 the simulated SWH coincides with T/P SWH quite well south of 17°N, with mean error less than 0.5 m. Along track 229 the simulated SWH is quite different from T/P SWH in the central SCS (5°–18°N). QSCAT wind speeds agree with T/P wind speeds quite well along track 190 south of

18°N, which leads to a better SWH simulation along that track. Wind speeds are quite different between QSCAT and T/P in the central SCS (8°–18°N) along track 229, which leads to larger SWH simulation errors along track 229.

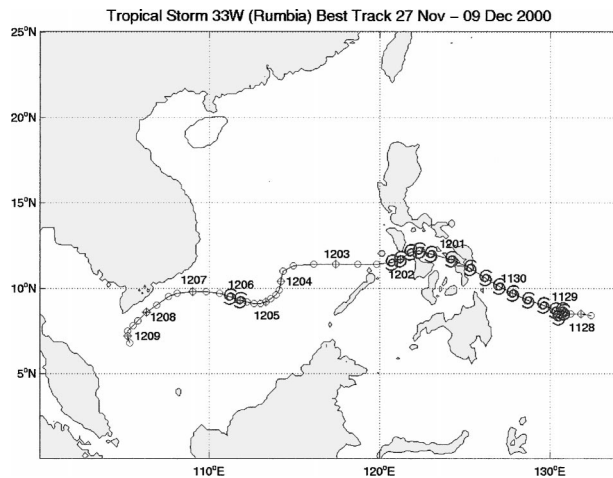Poor performance during Tropical Storm Rumbia may

FIG. 12. Track of Tropical Storm Rumbia (2000).

TABLE 2. Root-mean-square difference and maximum difference between QSCAT and T/P wind speeds.

Cycle No.	Track No.	No. of data pairs	Rms difference (m s^{-1})	Max difference (m s^{-1})
270	051	372	1.12	2.87
270	153	405	2.19	4.47
270	190	353	2.42	4.43
270	229	415	1.90	4.46
288	051	333	2.83	9.98
288	153	401	1.49	4.32
288	190	341	2.40	8.00
288	229	404	2.84	8.73
302	190	332	1.52	11.28
302	229	426	3.70	11.92
303	051	370	2.30	6.72
303	153	380	2.36	6.79

be caused by too-coarse grid resolution and lack of atmosphere–wave–ocean coupling. Chen et al. (2002) pointed out that simulation of typhoon or hurricane needs resolution from 1/6° for general structure to 2 km for detail eyewall structure. With the extreme high winds, intense rainfall, large ocean waves, and copious sea spray the surface flux parameterization should be updated. This is illustrated by numerical simulation of air–sea interaction under high wind conditions using a coupled atmosphere–ocean–wave modeling system (Bao et al. 2000). Improvement of WWATCH for high wind conditions needs finer resolution and more realistic parameterization for surface momentum flux.

d. Temporal error variability at selected crossover points

Understanding the temporal error variability, time series of H_m and H_o at four crossover points are presented (Fig. 14). WWATCH shows the capability in simulating SWH. Crossover point 2 (Fig. 14a) represents the southern SCS (Fig. 3). Bias, rmse, and cc at that point are 0.12 m, 0.41 m, and 0.92, respectively. The model errors do not have evident seasonal variability; that is, the model performance is equivalent during the prevailing monsoon seasons and during the monsoon transition periods.

Crossover point 6 represents the central SCS near 10°N (Fig. 3). Bias, rmse, and cc at that point are 0.03 m, 0.55 m, and 0.90, respectively. The model errors (Fig. 14b) are smaller during the (northeast) winter monsoon season (November–March) than during the (southwest) summer monsoon season (May–September).

Crossover point 11 represents the eastern part of the central SCS (15°N) near Luzon Island (Fig. 3). Bias, rmse, and cc at that point are 0.09 m, 0.49 m, and 0.90, respectively. Different from crossover point 6, the model errors (Fig. 14c) are larger during the (northeast) winter monsoon season (November–March) than during the (southwest) summer monsoon season (May–September). For example, the SWHs are all well predicted during the

summer monsoon season; however, during the winter monsoon period on 2 February the model-simulated SWH (3.27 m) is much larger than the observed SWH (2.10 m).

Crossover point 19 represents the north SCS near 20°N (Fig. 3). Bias, rmse, and cc at that point are 0.07 m, 0.43 m, and 0.94, respectively. The model errors (Fig. 14d) are larger during the (northeast) winter monsoon season (November–March) than during the (southwest) summer monsoon season (May–September). For example, the SWHs are all well predicted during the summer monsoon season; however, during the winter monsoon period on 7 December the model-simulated SWH (4.61 m) is much larger than the observed SWH (3.50 m).

e. Temporal error variability for the whole SCS

The monthly mean bias and rmse averaged over all of the crossover points in the SCS are presented in Fig. 15. They demonstrate the temporal error variability for the whole SCS tracks. WWATCH has very low bias (−0.01 to 0.04 m) in predicting SWH, with a maximum (positive bias) value of 0.04 m in March and a minimum (negative bias) value of −0.01 m in April. The rmse has a minimum value of 0.39 m in March and a maximum value of 0.48 m in December.

6. Uncertainty in surface wind data

Discrepancies between QSCAT and T/P wind speeds (right-hand panels of Figs. 10–13) are found especially during the Tropical Storm Rumbia period (1–9 December 2000), where the QSCAT winds are stronger than the T/P winds. Table 2 lists detail comparison between the two wind datasets. The root-mean-square difference between the two wind datasets increases from a minimum value of 1.12 m s^{-1} on 14 January 2000 (cycle 270, track 051) to a maximum value of 3.70 m s^{-1} on 3 December 2000 (cycle 302, track 229). The maximum difference between the two wind datasets increases from a minimum value of 2.87 m s^{-1} on 14 January 2000
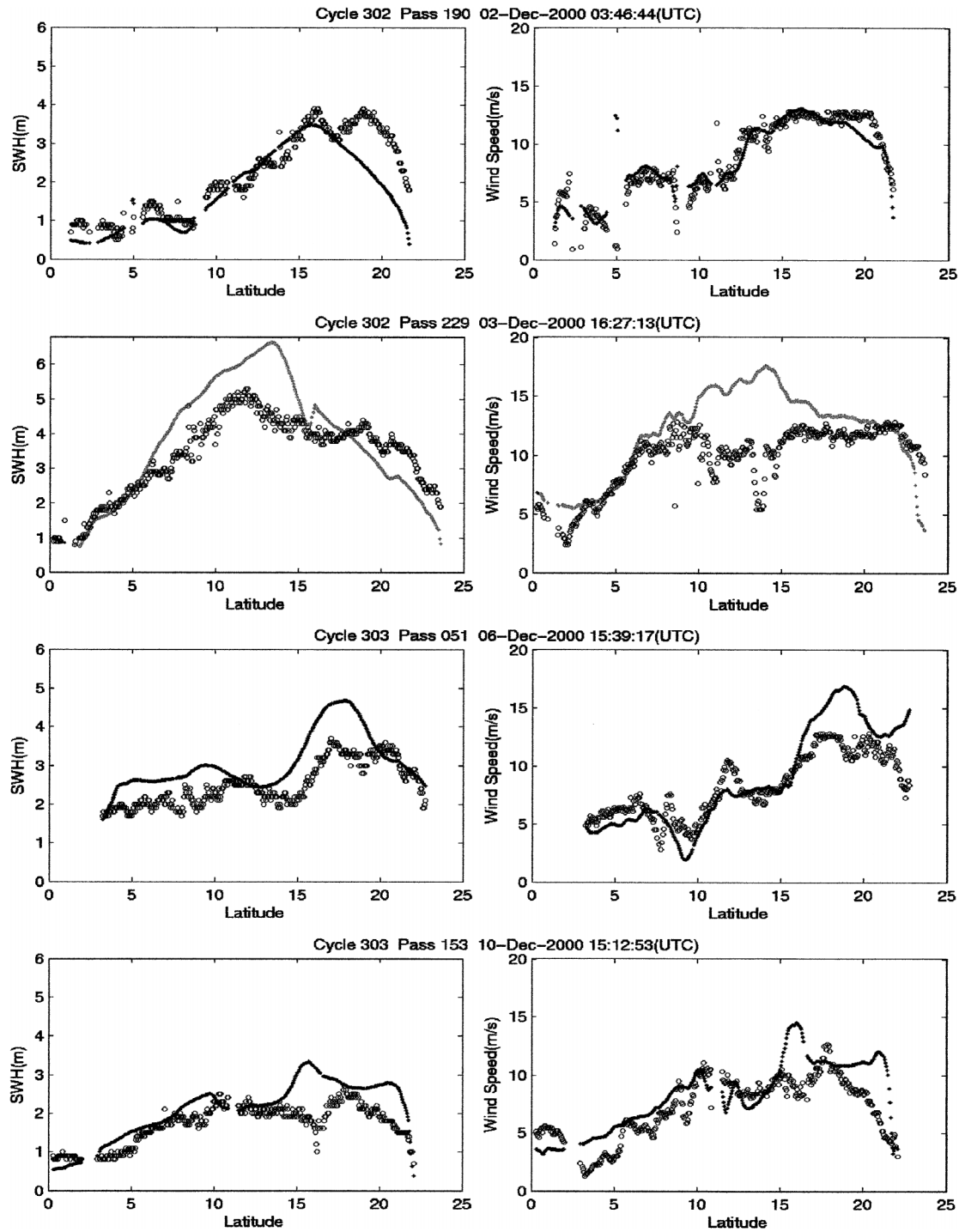
FIG. 13. Comparison between (left) modeled (dotted) and T/P observed (circle) SWHs and (right) QSCAT (dotted) and T/P observed wind speeds (circle) along the four tracks during cycles 302 and 303 (3–9 Dec 2000), when Tropical Storm Rumbia passed over the SCS.

(cycle 270, track 051) to a maximum value of 11.92 m s^{-1} on 3 December 2000 (cycle 302, track 229). Since the QSCAT winds are sensitive to rain, the large discrepancy during the Tropical Storm Rumbia (2000) period may be caused by heavy rain.

7. Conclusions

Comparing the South China Sea significant wave height hindcast using a third-generation wave model (Wavewatch-III) with significant wave height measured
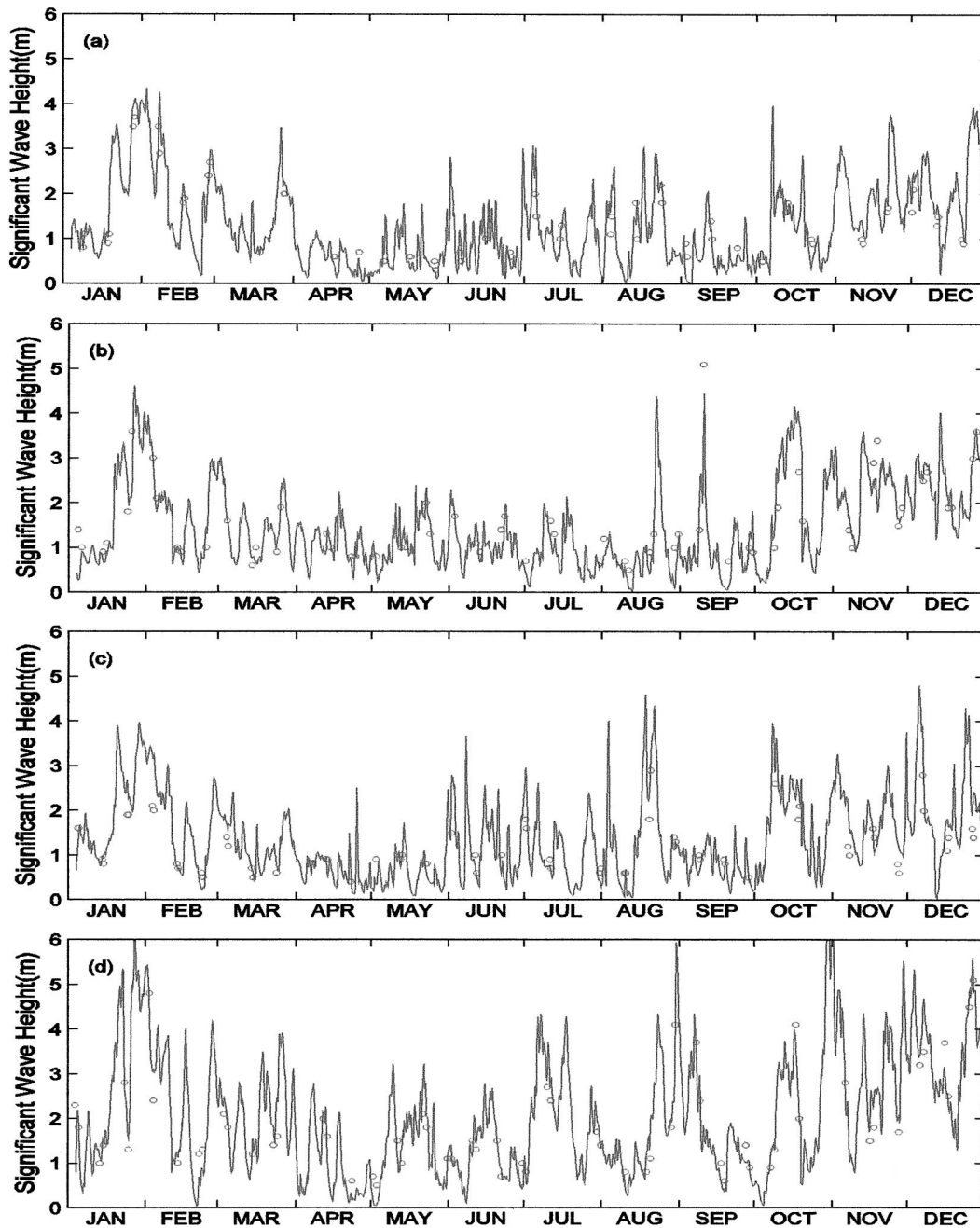
FIG. 14. Comparison between WWATCH modeled (solid curve) and T/P observed (denoted by circle) significant wave heights at (a) point 2, (b) point 6, (c) point 11, and (d) point 19.

by TOPEX/Poseidon altimeter for 2000, several characteristics of the model errors are obtained for the three subregions: the central, northern, and southern SCS.

1) Wavewatch-III simulates the seasonal variability of SWH reasonably well compared to the T/P SWH data. July 2000 SWHs are higher in the northern and central SCS (north of 10°N) than in the southern SCS (south of 10°N), with values up to 2.5 m in the WWATCH simulated field and 3.0 m in the observed

fields. The orientation of the high-SWH region coincides with the orientation of the monsoon winds.

2) The model errors for SWH hindcast have Gaussian-type distribution with mean values of 0.02 m and with slightly more sample numbers on the negative side (697) than on the positive side (633). The root-mean-square error and correlation coefficient between modeled and observed significant wave heights are 0.48 m and 0.90, respectively.

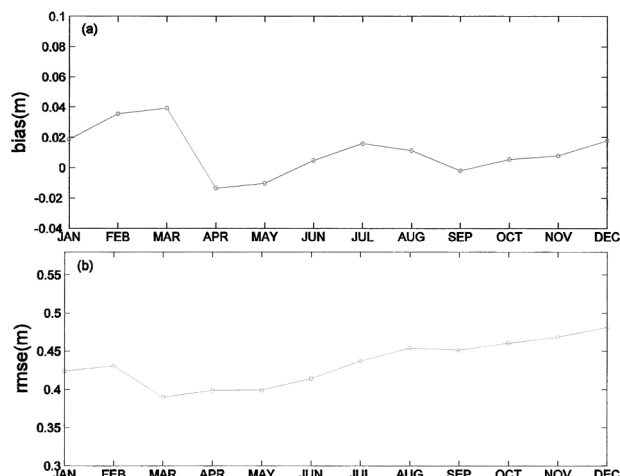3) The model errors of WWATCH have spatial vari-

FIG. 15. Temporal evolution of (a) bias and (b) rmse for the whole SCS.

ability with overprediction of the SWH, except on the shallow continental shelf. The rmse of SWH is above 0.5 m in the central SCS, with a maximum larger than 0.6 m west of Palawan. The value of rmse northward and southward decreases from the central SCS and is smaller than 0.5 m in most of northern (west of Luzon) and southern (south of 5°N) SCS.

4) Over the whole SCS, WWATCH has very low bias (-0.01 to 0.04 m) in predicting SWH, with a maximum (positive bias) value of 0.04 m in March and a minimum (negative bias) value of -0.01 m in April. The root-mean-square error has a minimum value of 0.39 m in March and a maximum value of 0.48 m in December.

5) The model errors are comparable to the T/P altimeter accuracy (0.5 m) in the central SCS and smaller than the T/P altimeter accuracy in the northern and southern SCS, which indicates the capability of Wavewatch-III for SCS wave simulation.

6) Ocean wave models are mainly forced by the surface winds. The difference between QSCAT and T/P wind speeds in this study indicates evident wind uncertainty. Modeling errors are caused by uncertain model external forcing (such as winds) or uncertain model internal structure (such as imperfect physics and resolution). Questions arise. What is the contribution of external and internal uncertainty on modeling errors? How does error propagate from winds to ocean waves? Will the wind error be amplified or damped after it enters the ocean wave models? We will answer these questions in the near future.

REFERENCES

Bao, J.-W., J. M. Wilczak, J.-K. Choi, and L. H. Kantha, 2000: Numerical simulation of air–sea interaction under high wind conditions using a coupled model: A study of hurricane development. *Mon. Wea. Rev.,* **128,** 2190–2210.

Booij, N., and L. H. Holthuijsen, 1987: Propagation of ocean waves in discrete spectral wave models. *J. Comput. Phys.,* **68,** 307–326.

Bretherthon, F. P., and C. J. R. Garrett, 1968: Wave trains in inhomogeneous moving media. *Proc. Roy. Soc. London A,* **302,** 529–554.

Callahan, P. S., C. S. Morris, and S. V. Hsiao, 1994: Comparison of TOPEX/POSEIDON σ_0 and significant wave height distributions to Geosat. *J. Geophys. Res.,* **99,** 25 015–25 024.

Chen, S. S., W. Zhao, J. E. Tenerelli, and M. Donelan, 2002: Atmosphere–wave–ocean coupling in tropical cyclones. Preprints, *25th Conf. on Hurricanes and Tropical Meteorology,* San Diego, CA, Amer. Meteor. Soc., 599–600.

Chu, P. C., S. H. Lu, and W. T. Liu, 1999a: Uncertainty of the South China Sea prediction using NSCAT and NCEP winds during tropical storm Ernie 1996. *J. Geophys. Res.,* **104,** 11 273–11 289.

——, N. L. Edmons, and C. W. Fan, 1999b: Dynamical mechanisms for the South China Sea seasonal circulation and thermohaline variabilities. *J. Phys. Oceanogr.,* **29,** 2971–2989.

——, J. M. Veneziano, and C. W. Fan, 2000: Response of the South China Sea to tropical cyclone Ernie 1996. *J. Geophys. Res.,* **105,** 13 991–14 009.

Dobson, E., F. Monaldo, and J. Goldhirsh, 1987: Validation of Geosat altimeter-derived wind speeds and significant wave heights using buoy data. *J. Geophys. Res.,* **92,** 10 719–10 731.

Fu, L. L., E. J. Christensen, C. A. Yamaone Jr., M. Lefebvre, Y. Menard, M. Dorrer, and P. Escudier, 1994: TOPEX/POSEIDON mission overview. *J. Geophys. Res.,* **99,** 24 369–24 381.

Hasselmann, D. E., M. Dunckel, and J. A. Ewing, 1980: Directional wave spectra observed during JONSWAP 1973. *J. Phys. Oceanogr.,* **10,** 1264–1280.

Hu, J.-Y., H. Kawamura, and D. L. Tang, 2003: Tidal front around the Hainan Island, northwest of the South China Sea. *J. Geophys. Res.,* **108,** 3342, doi:10.1029/2003JC001883.

Longuet-Higgins, M. S., and R. W. Stewart, 1961: The changes in amplitude of short gravity waves on steady non-uniform currents. *J. Fluid Mech.,* **10,** 529–549.

Pierson, W. J., and L. Moskowitz, 1964: A proposed spectrum from a fully developed wind seas based on the similarity theory of S. A. Kitaigorodskii. *J. Geophys. Res.,* **69,** 5181–5190.

Tolman, H. L., 1999: User manual and system documentation of WAVEWATCH-III version 1.18. NOAA/NCEP Tech. Note 166, 110 pp.

——, and D. V. Chalikov, 1996: Source terms in a third-generation wind wave model. *J. Phys. Oceanogr.,* **26,** 2497–2518.

——, and N. Booij, 1998: Modeling wind waves using wavenumber–direction spectra and a variable wavenumber grid. *Global Atmos. Ocean Syst.,* **6,** 295–309.

Whitham, G. B., 1965: A general approach to linear and non-linear dispersive, waves using a Lagrangian. *J. Fluid Mech.,* **22,** 273–283.

Wu, J., 1982: Wind stress coefficients over sea surface from breeze to hurricane. *J. Geophys. Res.,* **87,** 9704–9706.